# Buoyant finite-size particles in turbulent duct flow

Sagar Zade,[*] Walter Fornari, Fredrik Lundell, and Luca Brandt
*Linné Flow Centre, Swedish e-Science Research Centre, and KTH Mechanics, 100 44 Stockholm, Sweden*

Particle image velocimetry and particle tracking velocimetry have been employed to investigate the dynamics of finite-size spherical particles, slightly heavier than the carrier fluid, in a horizontal turbulent square duct flow. Interface resolved direct numerical simulations (DNSs) have also been performed with the immersed boundary method at the same experimental conditions, bulk Reynolds number $\mathrm{Re}_{2H} = 5600$, duct height to particle-size ratio $2H/d_p = 14.5$, particle volume fraction $\Phi = 1\%$, and particle to fluid density ratio $\rho_p/\rho_f = 1.0035$. Good agreement has been observed between experiments and simulations in terms of the overall pressure drop, concentration distribution, and turbulent statistics of the two phases. Additional experimental results considering two particle sizes $2H/d_p = 14.5$ and 9 and multiple $\Phi = 1\%, 2\%, 3\%, 4\%$, and 5% are reported at the same $\mathrm{Re}_{2H}$. The pressure drop monotonically increases with the volume fraction, almost linearly and nearly independently of the particle size for the above parameters. However, despite the similar pressure drop, the microscopic picture in terms of fluid velocity statistics differs significantly with the particle size. This one-to-one comparison between simulations and experiments extends the validity of interface resolved DNS in complex turbulent multiphase flows and highlights the ability of experiments to investigate such flows in considerable detail, even in regions where the local volume fraction is relatively high.

## I. INTRODUCTION

Particle-laden flows are widely encountered in environmental problems and industrial applications such as carriage of silt by rivers, drifting of snow, sorting of crushed materials, and transportation of nuclear waste. Since settling effects due to gravity are generally non-negligible in these flows, the understanding of the turbulence modulation mechanisms during particle transport under sedimentation is of practical importance. Among the many factors affecting turbulence modulation, particle size and density, volume fraction, fluid inertia, and particle-particle or particle-wall interaction are of extreme importance [1,2]. In this study we focus on the specific case of finite-size particle transport in a fully developed turbulent square duct flow. It also represents a reasonably complex wall-bounded case, for comparing simulations and experiments due to the presence of a mean secondary flow and the resulting nonhomogeneity in the duct cross section.

Point-particle simulations are often employed to study particle-laden flows. For the case of small heavy particles in a highly turbulent horizontal square duct flow, Yao and Fairweather [3] found that particle resuspension is promoted by the drag force arising from the secondary flows as well as shear-induced lift forces. Previously, Winkler *et al*. [4] simulated point particles in a vertical square duct and found that, in general, particles accumulate in regions of high compressional strain and low swirling strength. However, near the wall, the tendency of particles to accumulate in regions of high vorticity increases with particle response time. Sharma and Phares [5] showed that while

---

[*]zade@mech.kth.se

passive tracers tend to remain within the secondary flow, high-inertia particles accumulate close to the walls in a square duct. For a review on particle deposition and the entrainment mechanism from the wall in a turbulent flow, the reader is referred to [6].

The effect of finite-size sedimenting particles in a square duct was investigated by Lin *et al.* [7] for different Shields number $\text{Sh} = \tau_w/(\rho_p - \rho_f)d_pg$, which signifies the relative strength of shear forces $\tau_w d_p^2$ to buoyancy forces $(\rho_p - \rho_f)d_p^3g$ ($g$ being the acceleration due to gravity). Those authors observed that the presence of particles increases the secondary flow circulation, which in turn causes particles to accumulate preferentially at the face center of the bottom wall. Also, at constant $\Phi$ and pressure gradient, the flow rate decreases as the particle settling effect increased (lower Sh). It is also worth noting the recent simulations of Fornari *et al.* [8] for neutrally buoyant particles in a square duct up to a volume fraction of 20%. Those authors found that for $\Phi \leqslant 10\%$, particles preferentially accumulate on the corner bisectors and turbulence production is enhanced, whereas at $\Phi = 20\%$ particles migrate towards the core region and turbulence production decreases below the values for $\Phi = 5\%$. Shao *et al.* [9], in their channel flow simulations with settling particles, observed that when settling is significant enough, particles form a sediment layer that acts like a rough wall. Vortex structures shedding from this region ascend into the core and substantially increase the turbulence intensity there. Also, the effects of smaller particles on the turbulence are found to be stronger than those of larger particles at the same $\Phi$. Kidanemariam *et al.* [10] simulated turbulent open channel flow with low volume fractions of finite-size heavy particles. They found that particles show strong preferential concentration in the low-speed streaks due to quasistreamwise vortices, which result in particles moving, on average, slower than the average velocity of the fluid phase.

Experimental measurement of velocity and concentration field in suspensions is quite difficult, which has therefore limited our understanding of the interactions between the turbulent fluid and the near-mobile-bed region. Optical measurement techniques like particle image velocimetry (PIV) in suspension flows of finite-size particles rely on the use of particles that are transparent, i.e., the refractive indices of the fluid and particles are nearly the same with respect to the wavelength of the light used for illumination. However, the available particles are composed of materials like plastic, metal, glass, etc., which are usually opaque, and thus a volume fraction of 0.5% in a domain of 5–10 cm has been indicated as the limit [11]. Some limited options available for refractive-index-matching (RIM) fluids to enable the use of PIV can be found in [12]. However, they are often difficult to scale up due to issues related to long-time properties of the suspending solution, thermal stability, handling, and cost. Superabsorbent hydrogel particles in water, used in this study, can be advantageously used for performing RIM PIV as previously shown in [13–16]. The mechanical properties of commercially available spherical hydrogel particles are discussed in [17].

By performing fully resolved direct numerical simulations (DNSs) at the same bulk Reynolds number, particle size, density, and volume fraction as in experiments, we cross validate both tools and demonstrate the suitability of hydrogel particles to be used as rigid spheres in PIV experiments. Good agreement between experiments and simulations under the above conditions also indicate that the statistics in turbulent flow may not be very sensitive to the exact value of the collision and friction parameter required in simulations. Additional experiments for two particle sizes are presented here to estimate the turbulence modulation and particle dynamics as a function of the particle volume fraction.

## II. EXPERIMENTAL METHOD

The experiments are performed in a 5-m-long square duct with a $50 \times 50$ mm$^2$ cross section. The entire duct is made up of transparent acrylic permitting visualization throughout its length. Figure 1(a) shows a schematic of the flow loop. The fluid is recirculated through a closed loop consisting of a tank that is open to the atmosphere, where the particle-fluid mixture can be introduced. A static mixer (Vortab Company, San Marcos, CA, USA) in the form of an insertion sleeve is mounted inside the pipe section close to the inlet of the duct to neutralize swirling motions that may arise from the gradual 90° bend at the exit of the tank. It consists of a series of radial and
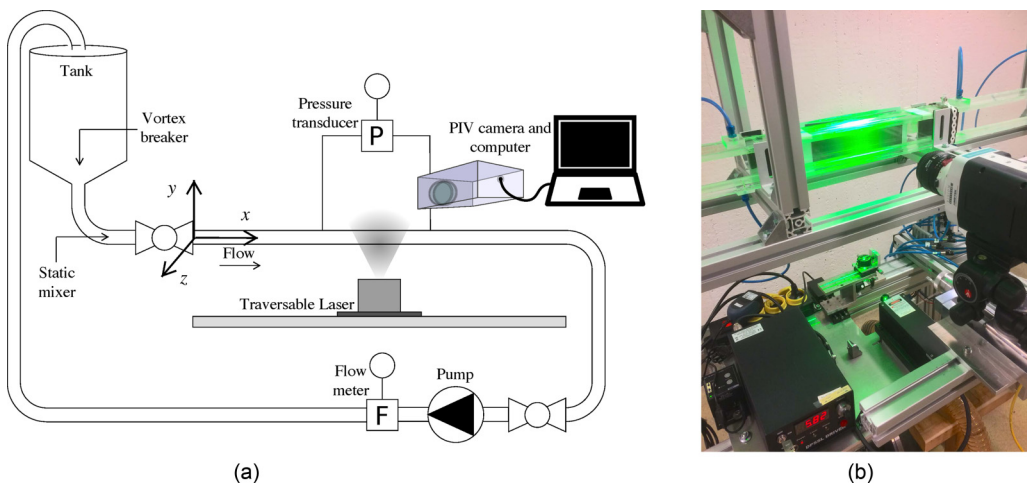
FIG. 1. (a) Schematic of the flow loop. (b) Photo of the section where PIV is performed.

inclined traverse tabs projecting from the inner surface of the conduit that promote cross-stream mixing. It is followed by a section providing a smooth transition from a circular to a square cross section. A tripping tape is installed at the entrance of the duct to trigger turbulence. The temperature is maintained at nearly $20°$C by means of an immersed-coil heat exchanger in the tank. In order to minimize mechanical breakage of the particles, a very gentle disk pump (Model No. 2015-8-2HHD, closely coupled, Discflo Corporation, Santee, CA, USA) has been chosen. It can handle solids up to a concentration of 40% for particles as large as 6 mm and has a pumping capacity up to 15 $m^3$/h without pulsations. A similar pump was previously used to study the laminar-turbulent transition in flow of polymer solution where the degradation of the polymer chains should be minimized to achieve high drag reduction for longer times [18].

An electromagnetic flow meter (Krohne Optiflux 1000 with an IFC 300 signal converter, Krohne Messtechnik GmbH, Germany) is used to measure the volume-flow rate of the particle-fluid mixture. Since the hydrogel particles are over 99% water, their electric and magnetic properties are similar to those of water. Hence, the flow rate measured by the electromagnetic flow meter is expected to be equal to the flow rate of the mixture. To reduce the risk of faulty readings caused due to electrical disturbances by particles in the flow meter, another flow meter with a ceramic electrode is also tested. The increase in the level of noise is marginal and as also reported in our earlier work [19], the results compared at different particle concentrations (up to $\Phi = 20\%$) and flow rates indicate a deviation less than 1% between the two flow meters. It can also be noted from [20] that the important aspect for the proper operation of electromagnetic flow meters in multiphase flows is that the mixture is fluid continuous, so that it is electrically conducting and small variations of conductivity have little effect (which is particularly true up to $\Phi = 40\%$ of the nonconducting dispersed phase). The Reynolds number $\mathrm{Re}_{2H}$, used hereafter, is based on the average or bulk velocity $U_{\mathrm{bulk}}$, the kinematic viscosity of the fluid $\nu_f$, and the duct height $2H$. The pressure drop is measured at a streamwise distance of nearly $140H$ from the inlet (the turbulent flow is seen to be fully developed at this entry length), across a length of $54H$ using a differential pressure transducer (0–1 kPa, Model No. FKC11, Fuji Electric France, S.A.S.). Data acquisition from the camera, flow meter, and pressure transducer is performed using a National Instruments NI-6215 DAQ card using Labview$^{\mathrm{TM}}$ software. Additional details can be found in [19].

## A. Particle properties

The particles are commercially procured superabsorbent (polyacrylamide-based) hydrogel spheres which are delivered in dry condition. They are graded into different sizes using a range

of sieves from which two sizes are selected for these experiments. Once mixed with tap water and left submerged for around one day, they grow to two equilibrium sizes, $3.5 \pm 0.8$ mm (3 times the standard deviation) and $5.60 \pm 0.9$ mm, yielding a duct height to particle diameter ratio $2H/d_p$ of 14.5 and 9, respectively. These two particles are referred to as smaller particles (SPs) and larger particles (LPs), respectively. The particle size is determined both by a digital imaging system and from the PIV images of particles in flow and a small spread in the particle diameter is observed. The fact that a Gaussian-like particle-size distribution has a small effect on the flow statistics has been shown in [21]. To retain the matching of refractive indices of the particle and fluid and at the same time facilitate the detection of particles in the PIV images, a small amount of fluorescent rhodamine (in ppm) was added to the water in which the particles expand. This enhances the contrast of the particles in the PIV images (shown later).

The density of the particles is determined using two methods: (i) by measuring the volume displacement by a known mass of particles and (ii) by determining the terminal settling velocity in a long liquid settling column. In the first method, a known mass of fully expanded particles is put in a water-filled container of uniform diameter. The rise in the level of water due to the particles is measured using a very precise laser distance meter (optoNTDC 1710, Micro-Epsilon Messtechnik GmbH, with a resolution of 0.5 $\mu$m). In the second method, a single particle with a known diameter is gently dropped in a long and wide cylindrical vertical column filled with water and the settling velocity is determined (after it has reached steady state). The particle is carefully released at the center of the column and away from the edges in order to minimize the edge effects. Also, the small-particle Reynolds number (based on the terminal velocity) implies that the wake behind the particle is steady axisymmetric [22], thus ensuring that it falls straight close to the centerline of the column. Owing to the relatively small opening at the top of the settling column compared to its volume, evaporative cooling is very small and hence the water inside the column is in thermal equilibrium with the walls of the column. Thus, secondary flows due to thermal convection are expected to play an insignificant role in the dynamics of the falling sphere. The small size of the particle $d_p$ relative to the diameter of the column $D$ ($d_p/D \leqslant 7\%$ and the length of the column is approximately equal to $600d_p$) implies that confinement effects by the column walls are negligible and empirical relationships that are applicable for free settling of a single sphere in an infinite fluid can be reasonably used. In fact, the increase in the drag coefficient due to edge effects for the above particle compared to falling in an unbounded medium is around 5% [23]. This translates to an underestimation of particle density by 0.02% if the relation for drag force $F$ on a settling particle

$$\frac{F}{\rho_f U_T^2 A} = \frac{12}{\mathrm{Re}_p}\big(1 + 0.15\,\mathrm{Re}_p^{0.687}\big) \tag{1}$$

is used to relate the particle diameter $d_p$ and terminal velocity $U_T$ to the unknown particle density $\rho_p$ [1]. The above relation is applicable in the transitional regime $1 < \mathrm{Re}_p < 750$. Here $A$ is the projected area of the particle in the falling direction. In Eq. (1), $\mathrm{Re}_p$ is the particle Reynolds number given by $\rho_f U_T d_p/\mu_f$, where $\mu_f$ is the dynamic viscosity of the liquid. Both of the above tests are performed at a room temperature of around 20 °C. The terminal velocity method yields a density ratio $\rho_p/\rho_f$ of $1.0035 \pm 0.0003$, whereas the volume displacement method yields a mean density ratio of 1.0030, albeit with higher uncertainty due to the very high sensitivity of the laser distance meter. The former method is preferred as it was more repeatable, being less sensitive to measurement uncertainties, and the corresponding value of density ratio is used for subsequent analysis.

In order to get an idea about the rigidity of the hydrogel particles, the restitution coefficient of the spheres is calculated in air by dropping a stationary particle on a flat thick acrylic sheet from a height of 0.1 m and the value is found to be around 0.9. Here the corresponding impact speed would be $\sqrt{2g\Delta h} = \sqrt{2 \times 9.81 \times 0.1} = 1.4$ m/s. With higher impact speeds, we observe that deformation and losses lead to lower values of the coefficient of restitution. However, for the typical low velocities ($U_{\mathrm{bulk}} \approx 0.1$ m/s) and corresponding low dynamical forces in the present flow configuration, the hydrogel particles do not exhibit any visible deformation (as also confirmed from time-resolved movies of the particles in flow). In water, the coefficient of restitution would be

different due to the higher viscous dissipation in the liquid as compared to air, and as pointed out by Gondret *et al.* [24], the coefficient of restitution is a function of the particle Stokes number $St = \rho_p Re_p / 9 \rho_f$, where the particle Reynolds number $Re_p = U d_p / \nu_f$ is based on the impact velocity $U_p$, and thus St is a function of the impact velocity between two colliding particles or between a particle and the wall. If the typical impact velocity is assumed to be of the order of the rms of the fluid velocity fluctuations (which is also close to the particle terminal velocity), the particle Stokes number in water turns out to be approximately equal to 4 and as observed in many previous studies (e.g., [24,25]), for $St \leqslant 10$ collisions are dominated by viscous effects and particles do not rebound, i.e., the effective coefficient of restitution will be very small.

### B. Velocity measurement: PIV plus particle tracking velocimetry

The coordinate system used in this study is indicated in Fig. 1(a) with $x$ the streamwise, $y$ the wall-normal, and $z$ the spanwise directions. The velocity field is measured using two-dimensional PIV in three spanwise planes: $z/H = 0$, 0.4, and 0.8. These measurements are performed at a streamwise distance of $x/H \approx 150$ from the entrance of the duct.

A continuous-wave laser (wavelength equal to 532 nm and power equal to 2 W) and a high-speed camera (Phantom Miro 120, Vision Research, Wayne, NJ, USA) are used to capture successive image pairs. The thickness of the laser light sheet is 1 mm. Figure 1(b) shows the PIV setup.

For imaging the full height of the duct, a resolution of approximately 60 mm/1024 pixels is chosen. The frame rate (acquisition frequency) is chosen so that the maximum pixel displacement, based on the mean velocity, does not exceed a quarter of the size of the final interrogation window (IW) [26]. Images are processed using an in-house, three-step, fast-Fourier-transform-based, cross-correlation algorithm [27]. The first step consists of basic PIV with a large IW size ($48 \times 48$ pixels), followed by the discrete-window-shift PIV at the same IW size, and finally, the central-difference-image-correction method [28] with the final IW size ($32 \times 32$ pixels). The maximum pixel displacement is around 12 pixels. Regarding the subpixel interpolation, we use a three-point Gaussian subpixel estimator [26]. As noted in [27], the accuracy of the in-house PIV algorithm is estimated using artificial particle images [29] and uncertainty in evaluation of the particle displacement is approximately 0.2 pixels. The degree of overlap is around 47% and can be estimated from the fact that the corresponding final resolution is $1 \times 1$ mm$^2$ per IW. Additional near-wall measurements are conducted by zooming in the camera on a small region close to the wall with a resolution that is approximately 3 times higher. Each experiment is repeated at least 3 times and 500 image pairs are observed to be sufficient to ensure statistically converged results.

Figure 2(a) depicts one image (A) from a typical PIV sequence (A → B) for particle-laden flow. As mentioned earlier, the contrast between particle and fluid is enhanced by using a small quantity of rhodamine. Raw images captured during the experiment are saved in groups of two different intensity levels as follows. The first group of images, designated as PIV-A plus PIV-B with a typical example of PIV-A being shown in Fig. 2(a), is used for regular PIV processing according to the algorithm mentioned above to find the fluid velocity field. The same first group of images is later contrast enhanced in the postprocessing step and constitutes the second group of images. This second group of images, designated as PTV-A plus PTV-B with an example of PTV-A being shown in Fig. 2(b), is used for detecting the particles only. Thus, PIV-A and PTV-A denote the same time instance but differ in their intensity levels.

Once the images are recorded, the following steps are followed during postprocessing to transform the image in Fig. 2(a) to something like the image in Fig. 2(b). First, the potential particles are made brighter and the surrounding fluid is made darker by adjusting the *sensitivity* and *flare* options in the Phantom Camera Control software (version 2.8.761.0). Later, the local-average-minimum-intensity background is subtracted from each image so as to get rid of the reflections from the top and bottom walls. Next a pixelwise adaptive low-pass Wiener filter is used in MATLAB™ to remove the small bright tracer particles from the image. To prevent false particle detection, due to large intensity gradients occurring near the walls, the region beyond the walls is masked with a
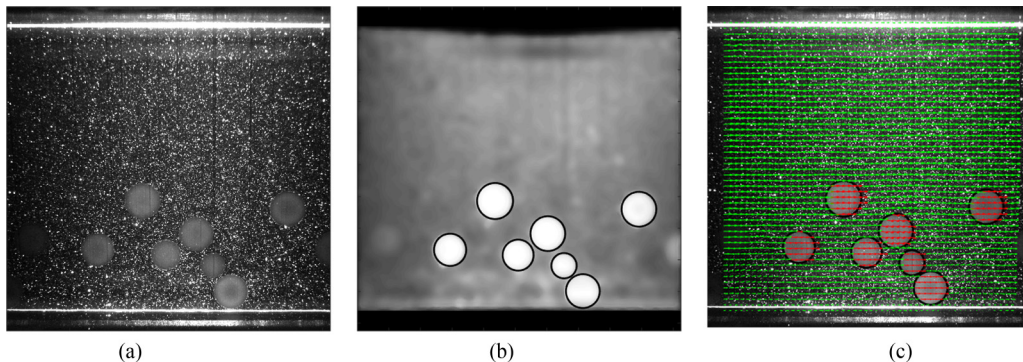
FIG. 2. (a) Raw image for PIV, (b) enhanced image for particle tracking velocimetry (PTV), and (c) resultant PIV (green, in fluid phase) plus PTV (red, in particle phase) velocity vectors. The above example corresponds to large particles at $\Phi = 3\%$. Note that the particle region is encircled with a solid black line in (b).

zero-intensity value. Particles are detected using a circular Hough transform [30] by specifying a range of expected particle size ($0.5d_p$, $1.3d_p$). Detected particles whose average intensity level lies below 70% of the average intensity of all detected particles are ignored.

From the detected particles in images PTV-A and PTV-B of the sequence, a nearest-neighbor approach is used to determine their translational motion. The nearest-neighbor approach used for PTV is rather simple and readily works because the average displacement of a particle between two time frames is substantially smaller (less than 15 pixels) compared to the distance between the centers of two neighboring particles (greater than 30 pixels). Accordingly, the Cartesian distances between the center of area of a reference particle in frame PTV-A and all particles in frame PTV-B are calculated. The particle with the minimum distance, lower than a threshold of 20 pixels, is chosen as a match for the reference particle and the corresponding velocity is calculated. The same procedure is repeated for all the remaining particles in frame PTV-A. Particles in PTV-A that find no matching candidate in PTV-B, due to out-of-plane motion or motion beyond the field of view, are thus eliminated by the PTV algorithm.

For the Eulerian PIV velocity field, we define a mask matrix, which assumes the value 1 if the point lies inside the particle and 0 if it lies outside. The fluid phase velocity is thus determined on a fixed mesh. The particle velocity is determined using PTV at its center, which is assigned to the grid points inside the particle (mask equal to 1). The velocity field of the particle phase is now available at the same grid points as that of the fluid and the ensemble averaging, reported later, is phase-averaged statistics. Figure 2(c) shows the combined fluid (PIV) and particle (PTV) velocity field. Owing to the curvature of the particles, it is possible that IWs close to the particle boundary have a contribution in velocity from the particle phase and hence some particle-fluid averaging may ensue. To circumvent this issue, we try calculating the fluid statistics by ignoring one layer of PIV points around the particle, but no significant difference is observed in the long-time statistics as compared to no omission. Hence, it can be said that bias introduced by the particles to the fluid phase velocity is small.

## III. NUMERICAL SETUP AND METHODOLOGY

The DNSs have been performed using the immersed boundary method (IBM), originally developed by Breugem [31], which fully models the coupling between the solid and fluid phases. The flow evolves according to the incompressible Navier-Stokes equations, whereas the particle motion is governed by the Newton-Euler Lagrangian equations for the particle linear and angular velocities. Using the IBM, the boundary condition at the moving fluid-solid interfaces is modeled
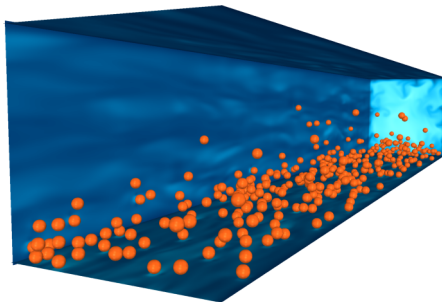
FIG. 3. Instantaneous snapshot of the magnitude of the near-wall fluid streamwise velocity together with the particles. The solid volume fraction $\Phi = 1\%$.

by an additional force on the right-hand side of the Navier-Stokes equations, making it possible to discretize the computational domain with a fixed staggered mesh on which the fluid phase evolves using a second-order finite-difference scheme. Time integration is performed by a third-order Runge-Kutta scheme combined with pressure correction at each substep. When the distance between two particles becomes smaller than twice the mesh size, lubrication models based on Brenner's asymptotic solution [32] are used to correctly reproduce the interaction between the particles. A soft-sphere collision model is used to account for collisions between particles. An almost elastic rebound is ensured with a restitution coefficient set at 0.97. As stated previously, since the particle Stokes number during impact is less than 10, collisions are dominated by viscous effects and particles do not rebound [24,25]. Hence, in simulations the important role of the collision model is to ensure that particles occupy their own volume, i.e., once particles are in the imminence of contact, they cannot overlap. Then the solid-fluid coupling will dictate the turbulence modulation by the presence of particles. More details and validations of the numerical code are provided in previous publications [8,33,34].

The simulations are performed in a Cartesian computational domain of size $L_x = 12H$, $L_y = 2H$, and $L_z = 2H$. The domain is discretized by a uniform mesh ($\Delta x = \Delta y = \Delta z$) of $2592 \times 432 \times 432$ Eulerian grid points in the streamwise and crossflow directions. The bulk velocity of the entire mixture is kept constant by adjusting the streamwise pressure gradient to achieve a constant bulk Reynolds number $\mathrm{Re}_{2H} = 5600$. The volume fraction $\Phi = 1\%$ corresponds to 353 particles. The number of Eulerian grid points per particle diameter is 30 ($\Delta x = 1/24$). The gravitational forces acting on the particle with respect to fluid viscous forces are quantified by the Galileo number $\mathrm{Ga} = \sqrt{(\rho_p/\rho_f - 1)g(d_p^3)/\nu_f^2}$ equal to 40 for the particles simulated ($2H/d_p = 14.5$ and $\rho_p/\rho_f = 1.0035$). The particle Shields number $\mathrm{Sh} = 0.45$, based on the shear stress for single-phase flow.

Figure 3 shows an example of the instantaneous particle distribution in the computational domain. From the near-wall streamwise velocity, the signature of near-wall streaks can be more prominently seen for walls other than the bottom wall where particle concentration is high. For the bottom wall, hot spots of higher fluid streamwise velocity are seen below each particle. The statistics are collected after the initial transient phase of $490H/U_{\mathrm{bulk}}$, using an averaging period of $1040H/U_{\mathrm{bulk}}$.

## IV. RESULTS

We first compare the results of the DNS code with the experimental measurements for single-phase flow at $\mathrm{Re}_{2H} = 5600$. Then we discuss the results from DNSs and experiments for smaller particles at a volume fraction $\Phi = 1\%$. Finally, we present purely experimental results for $\Phi = 1\%$, 2%, 3%, 4%, and 5% for SPs and LPs.
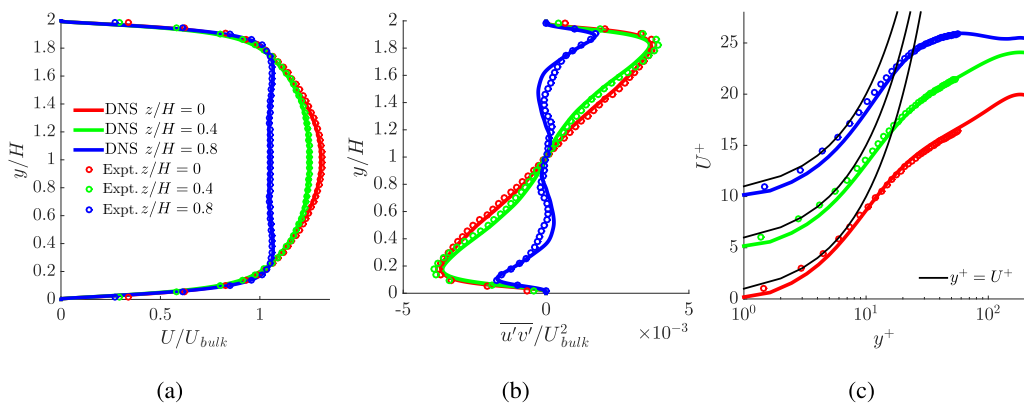
FIG. 4. Single-phase velocity statistics: (a) mean streamwise velocity, (b) primary Reynolds shear stress scaled in bulk units ($U_{\text{bulk}}$ and $2H$), and (c) mean streamwise velocity scaled in inner units ($u_\tau$ and $\nu/u_\tau$). In (c), the plots for successive spanwise planes are shifted upward by $5U^+$ units for better visualization).

### A. Single-phase-flow validation

Figures 4(a) and 4(b) show the streamwise velocity and the corresponding Reynolds shear stress for the single-phase flow measured at three different spanwise planes: $z/H = 0$, 0.4, and 0.8. It is well documented that the gradient in the Reynolds stresses leads to a secondary flow of Prandtl's second kind in the duct (see [35]). This secondary motion appears in the form of four pairs of counterrotating vortices near the duct corners, driving high-speed fluid from the center of the duct towards the corners and low-speed fluid from the wall towards the center. This redistribution of momentum is reflected in the streamwise velocity profiles of Fig. 4(a). The measured mean streamwise and fluctuating velocity statistics are in good agreement with those of the simulations. The maximum deviation appears in the second-order turbulent statistics in the $z/H = 0.8$ plane due to the proximity of this plane to the sidewall ($z/H = 1$). This is because, in this near-wall region, the shear rate and turbulence intensity are relatively high, leading to larger out-of-plane motion and hence larger uncertainties in PIV measurements. Figure 4(c) shows again the mean streamwise velocity close to the bottom wall, now scaled in inner units, from separate measurements with higher resolution, where it is possible to measure velocity statistics from distances as small as $y^+ \approx 1.5$.

### B. Comparing experiments and simulations: Smaller particles ($2H/d_p = 14.5$) at $\Phi = 1\%$

The finite-size particles, while being carried forward by the surrounding fluid also sediment due to their relatively high density. They are often resuspended upward by instantaneous turbulent structures, local shear-induced lift, and collisions with neighboring particles. Thus, particles mostly occupy the bottom half of the duct and undergo a saltation type of motion [36], i.e., particles removed from the bottom wall are carried by the fluid, before being transported back to the wall.

Figure 5 shows the mean particle concentration [Figs. 5(a)–5(c)], fluid and particle mean streamwise velocity [Figs. 5(d)–5(f)], and fluid Reynolds shear stress [Figs. 5(g)–5(i)] for SPs at a volume fraction $\Phi = 1\%$. Each column corresponds to a spanwise plane starting from the plane of the wall bisector $z/H = 0$ [Figs. 5(a), 5(d), and 5(g)] to a plane near the sidewall $z/H = 0.8$ [Figs. 5(c), 5(f), and 5(i)].

Particles, on average, form a one-diameter-thick layer of high concentration in contact with the wall, as seen in the mean concentration profiles [Figs. 5(a)–5(c)]. Reduced concentration appears above the bottom layer. The concentration is maximum (peak value of approximately 10%) in the plane of the wall bisector $z/H = 0$ and drops towards the sidewall $z/H = 1$. With increasing bulk velocity, the concentration in the bottom layer will reduce until, at sufficiently higher velocities, all
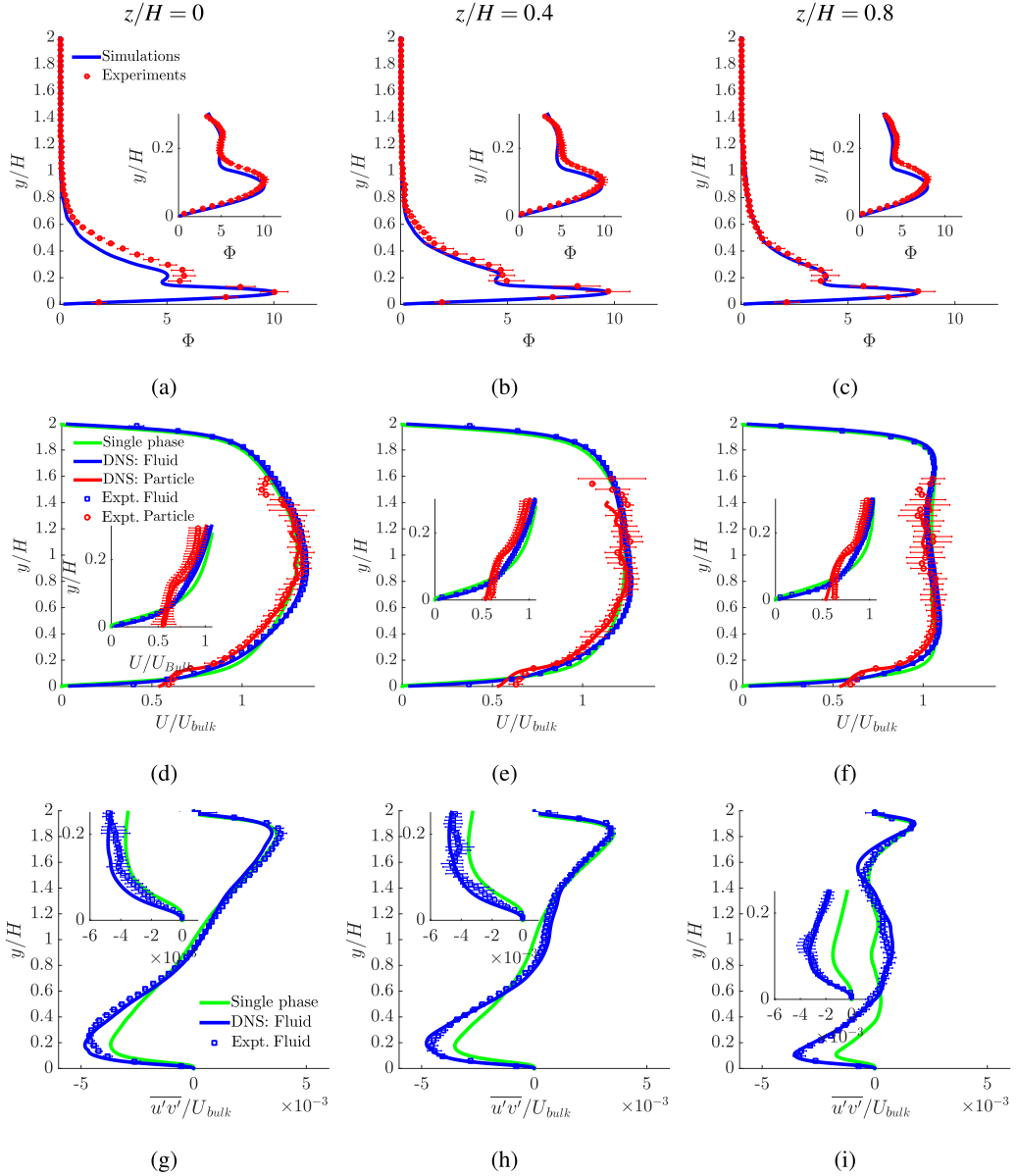
FIG. 5. Simulation and experimental results for SPs at $\Phi = 1\%$: (a)–(c) mean particle concentration, (d)–(f) mean streamwise velocity, and (g)–(i) primary Reynolds shear stress for three spanwise planes, namely, (a), (d), and (g) $z/H = 0$, (b), (e), and (h) $z/H = 0.4$, and (c), (f), and (i) $z/H = 0.8$.

the particles will be homogeneously distributed (see [19]). The concentration distribution measured experimentally is the area concentration in a two-dimensional slice whose thickness is equal to the thickness of the laser light sheet; the particle is recognized as the largest projection of a spherical section cut by the light sheet, hence the different apparent diameter of particles in Fig. 2(a). The conversion from such an area concentration to volume concentration is nontrivial and hence to maintain consistency between simulations and experiments, we normalize the experimental area concentration so that its maximum value equals the maximum of the volume concentration in DNSs.
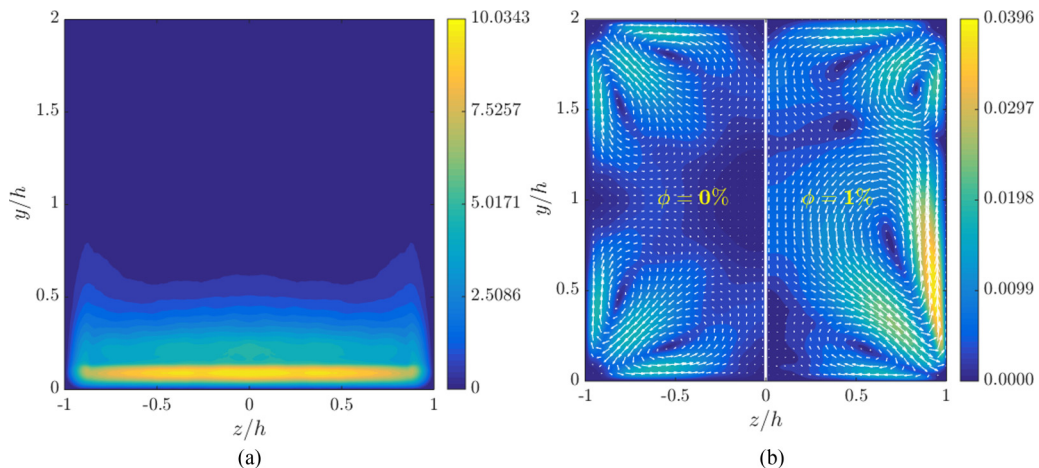
FIG. 6. (a) Particle concentration distribution (in percent) and (b) mean secondary fluid velocity $\sqrt{V^2 + W^2}/U_{\text{bulk}}$ from simulations. In (b), the left panel corresponds to single-phase flow $\Phi = 0\%$ and the right panel corresponds to $\Phi = 1\%$.

The insets in Figs. 5(a)–5(c) show the details of the high-particle-concentration region obtained by separate near-wall measurements.

The mean streamwise velocity of the fluid phase is skewed due to the asymmetry in the particle concentration when compared to the profile for the single-phase flow [Figs. 5(d)–5(f)]. The fluid velocity is reduced by the particle drag in the particle-rich region and this is compensated, in order to maintain the same volume-flow rate, by a proportional increase in the upper regions. On average, particles move slowly compared to the fluid nearly in the whole cross section, except close to the walls, where particles are not constrained by the no-slip condition limiting the fluid velocity to zero at the walls. The particle velocity is displayed without considering the particle rotation as it is not possible to measure particle rotation for our RIM particles. Early trials with tracer-embedded RIM particles as in [15] showed that even a small quantity of tracers severely reduce the optical visibility of the suspension and limit the applicability of PIV plus PTV in regions of high concentration. The apparent slip velocity is expected to be lower if rotation is also included while calculating particle velocity.

The fluid Reynolds shear stress is seen to increase when compared to the single-phase case in particle-dominated areas [Figs. 5(g)–5(i)] in all three spanwise planes. The enhanced fluid Reynolds shear stress is indicative of increased mixing of the fluid phase in this region. For this low volume fraction $\Phi = 1\%$, the Reynolds shear stress approaches the values of the single-phase flow in the particle-free upper region of the duct. The mean velocity profile in this region also remains similar to the single-phase case.

Overall, we find reasonable agreement between numerical and experimental results in terms of particle concentration and velocity statistics. Also, the pressure drop, shown later, is seen to agree quite well.

Additional details regarding the flow can be obtained from Fig. 6, where we present the mean particle distribution and the mean secondary motion for the fluid phase, from simulations, for the entire cross section of the duct. As shown in Fig. 6(a), particles are suspended at higher elevations near the two sidewalls ($z/H = -1$ and 1), most likely owing to an enhanced secondary flow as shown in Fig. 6(b). In the single-phase flow, the peak magnitude of this secondary motion $\sqrt{V^2 + W^2} \approx 0.02 U_{\text{bulk}}$. In the presence of particles, this peak value increases to approximately $0.04 U_{\text{bulk}}$ and occurs closer to the sidewalls, thus causing particles to rise upward in that region. Due to the higher concentration of particles near the bottom wall, the secondary flow is no longer symmetric along the vertical direction, as also previously observed in [7].

TABLE I. Cases investigated.

| $2H/d_p$ | $\Phi$ (%) | Studies performed |
|---|---|---|
| 14.5 | $1 \pm 0.1$ | PIV plus PTV and DNS |
| 14.5 | $1, 2, 3, 4, 5 \pm 0.1$ | PIV plus PTV |
| 9 | $1, 2, 3, 4, 5 \pm 0.1$ | PIV plus PTV |

### C. Effect of particle size and volume fraction

A summary of the different experiments performed is listed in Table I. The $\mathrm{Re}_{2H} = U_{\mathrm{bulk}} 2H/\nu_f$ in experiments is maintained at $5660 \pm 150$ across all cases. The ratio of the particle terminal velocity $U_T$ to the bulk velocity $U_{\mathrm{bulk}}$ is 0.08 and 0.13 for SPs and LPs, respectively. To quantify the role of gravity in the mode of particle transport, the Rouse number $\mathrm{Ro} = U_T/\kappa u_\tau$ [37] is often used. Here $\kappa$ is the von Kármán constant and $u_\tau = \sqrt{\tau_w/\rho_f}$ is the friction velocity for single-phase flow with $\tau_w$ the average wall-shear stress estimated from the streamwise pressure gradient: $\tau_w = (dP/dx)(H/2)$. In our experiments, Ro is around approximately 3 and 5 for SPs and LPs, which corresponds to bed load transport, i.e., particles transported along the bed ($\mathrm{Ro} \geqslant 2.5$) [38]. The particle Stokes number $\mathrm{St} = (\rho_p d_p^2/18\rho_f \nu_f)/(H/U_{\mathrm{bulk}})$ based on the fluid bulk timescale is approximately equal to 3 and 8 for SPs and LPs, respectively. Finally, the particle size in inner length scales of the single-phase flow for the small particles is approximately $25\delta_\nu$ (where $\delta_\nu = \nu/u_\tau$ is the viscous length scale) and approximately $40\delta_\nu$ for the large particles. So the SPs are already around 5 times larger than the thickness of the viscous sublayer.

#### 1. Pressure drop

The pressure drop, expressed as the friction Reynolds number $\mathrm{Re}_\tau = u_\tau H/\nu_f$, is plotted in Fig. 7 as a function of particle volume fraction $\Phi$. As expected, $\mathrm{Re}_\tau$ increases with increasing $\Phi$. Within the limits of the error bars, particles of both sizes result in similar values of the pressure drop. The pressure drop predicted by DNS for $\Phi = 1\%$ of SPs (stars in Fig. 7) is also close to the experimentally measured value. The small offset between DNSs and experiments with the particle-laden case is of the same order as the difference in the single-phase case, i.e., less than 2%.
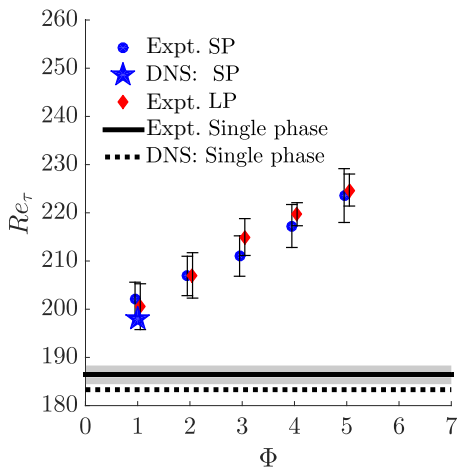


FIG. 7. Friction Reynolds number at bulk $\mathrm{Re}_{2H} = 5600$ as a function of the particle size and volume fraction.
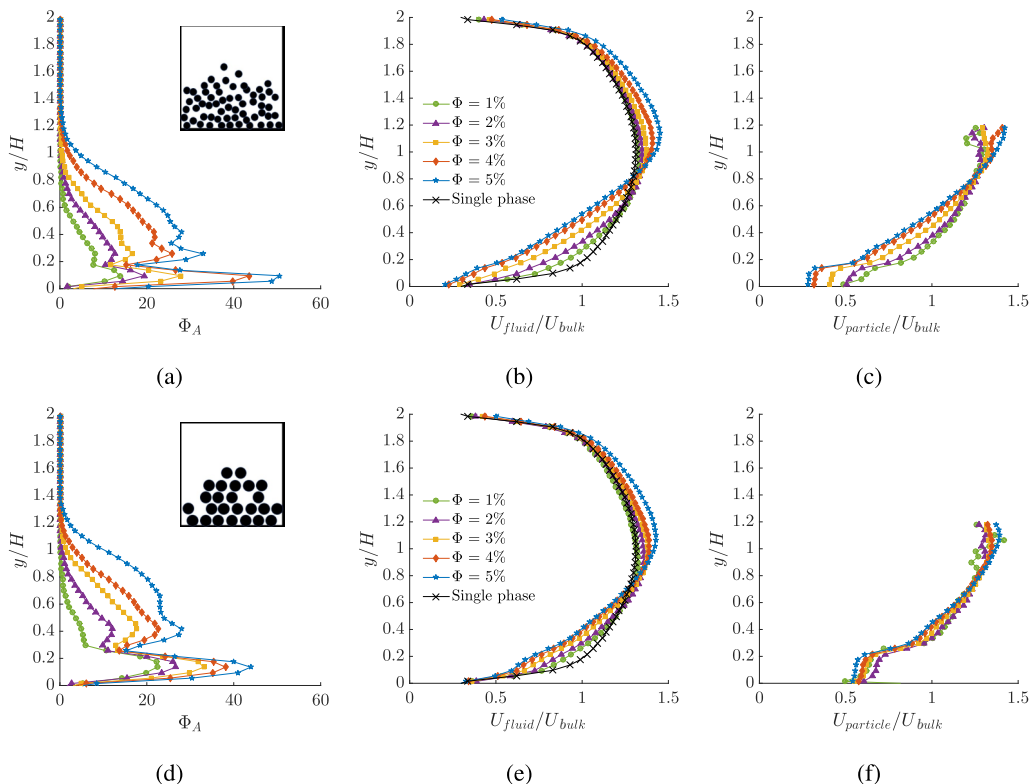
FIG. 8. Particle concentration and mean velocity at $z/H = 0$: (a) and (d) mean particle concentration, (b) and (e) mean fluid streamwise velocity, and (c) and (f) mean particle streamwise velocity for (a)–(c) smaller particles and (d)–(f) larger particles. The relative size and distribution of the particles are illustrated by the cartoon in the corresponding inset in (a) and (d).

## 2. Concentration and velocity distribution

Even though the overall pressure drop is very similar for the two particle sizes and seems mainly to be a function of the concentration, noticeable differences are seen in the turbulent velocity statistics of the fluid phase. Figure 8 shows the mean particle area concentration $\Phi_A$ and mean fluid and particle streamwise velocity for SPs [Figs. 8(a)–8(c)] and LPs [Figs. 8(d)–8(f)] in the plane of the wall bisector $z/H = 0$. The concentration distribution is similar for both particle sizes for all bulk volume fractions [Figs. 8(a) and 8(d)]. The thickness of the particle layer is higher for LPs due to their larger size. With an increase in nominal volume fraction, a second layer of high particle concentration appears above the first one and at the highest concentration $\Phi = 5\%$, there is a tendency for a third layer, more so for SPs due to their larger number $N \propto \Phi/d_p^3$. The maximum particle concentration reaches values above 40% and yet using RIM PIV, it is possible to measure velocity inside the flow, i.e., beyond 6–7 particle diameters.

Compared to the single-phase case, the mean fluid streamwise velocity is monotonically reduced by increasing $\Phi$ in the lower region where the particle concentration is high [Figs. 8(b) and 8(e)]. In this region, the mean velocity approaches a linear profile, or constant shear rate, for increasing $\Phi$. To maintain the same flow rate, the upper region experiences therefore higher velocity and the peak in the velocity profile is displaced upward with increasing $\Phi$. The above modification is more pronounced for SPs than for LPs. Particles, on average, move slower than the fluid phase [Figs. 8(c) and 8(f)], except close to the wall. For SPs, the apparent slip velocity in the near-wall region is lower
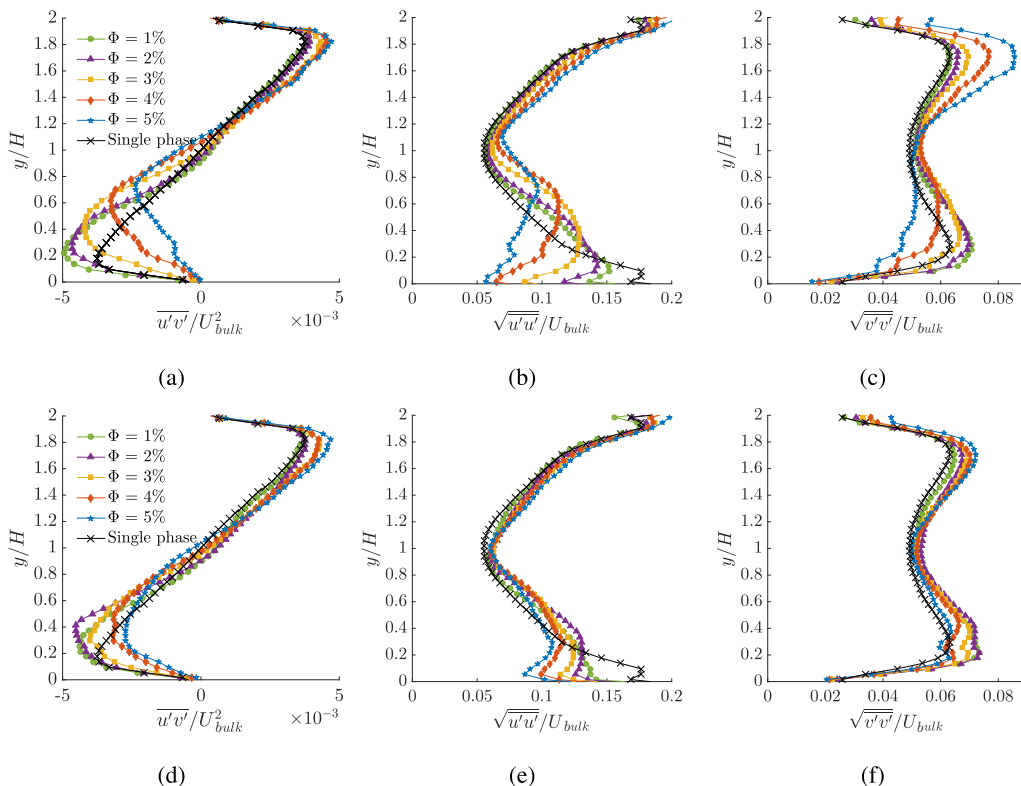
FIG. 9. Fluid velocity fluctuation statistics at $z/H = 0$: (a) and (d) primary Reynolds shear stress, (b) and (e) rms of the streamwise fluctuating velocity, and (c) and (f) rms of the wall-normal fluctuating velocity for results for (a)–(c) smaller particles and (d)–(f) larger particles.

than for LPs and decreases further with increasing $\Phi$. The lower velocity of SPs as compared to LPs is due to the fact that the bottom layer of SPs is exposed to lower fluid velocity. This reduction of particle velocity with $\Phi$ conforms with the reduced fluid velocity for the corresponding $\Phi$.

The fluid velocity fluctuation statistics are more significantly changed for SPs than for LPs (see Fig. 9), indicating that, for a given particle density and volume fraction, larger particle number has larger effects, as also observed by Shao *et al.* [9]. Those authors suggested that at the same $\Phi$, the fluid inertial effects are more pronounced for particles with a larger number density, i.e., smaller particles are more effective than larger particles. Also, the area on the wall occupied by SPs ($\sim Nd_p^2 \propto \Phi/d_p$) is larger than for LP, causing larger hindering effects for the near-wall fluid structures.

For $\Phi = 1\%$ and $2\%$, the negative peak in the fluid Reynolds shear stress [Figs. 9(a) and 9(d)] increases. With increasing $\Phi$, the location of this peak is displaced away from the wall, again more for SPs than for LPs. For $\Phi$ larger than $3\%$, the Reynolds shear stress is increasingly suppressed in the lower (near-wall) part of the particle-rich region while it increases in the upper part of the duct until it approaches values similar to or slightly higher than the single-phase case in the particle-free region.

Similar behavior is seen for the rms of the streamwise velocity fluctuations: These are increasingly suppressed in the lower part of the duct, more for SPs than for LPs, followed by an increase before finally approaching values similar to or slightly higher than the single-phase case. Suppression of turbulent velocity fluctuations by increasing $\Phi$ of inertial-range-size particles has also been observed in [14], albeit in the configuration of the von Kármán swirling flow. The rate of
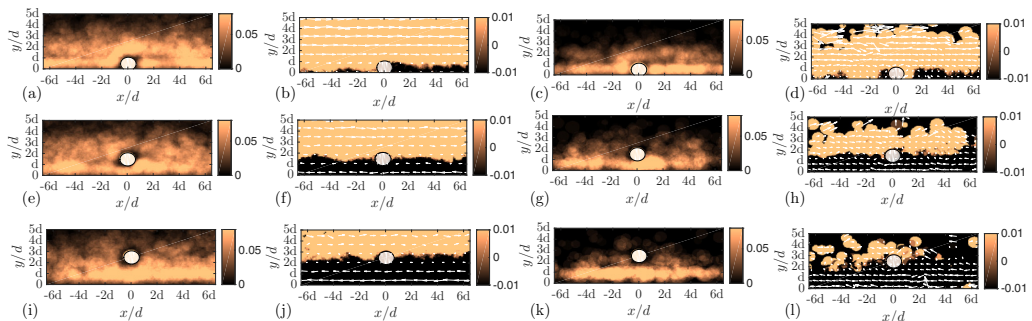
FIG. 10. Concentration and relative velocity distribution around a reference particle at $\Phi = 1\%$ for both SPs and LPs. The three rows corresponds to three layers of particles: (a)–(d) bottom near-wall layer, (e)–(h) second layer above the wall, and (i)–(l) third layer above the wall for the (a), (e), and (i) particle-centered concentration distribution for SPs, (b), (f), and (j) relative streamwise velocity for SPs, (c), (g), and (k) particle distribution for LPs, and (d), (h), and (l) relative streamwise velocity for LPs. The white arrows in the second and fourth columns represent the net relative velocity $U_{\rm rel}\hat{x} + V_{\rm rel}\hat{y}$.

reduction was found to be slower (proportional to $\Phi^{2/3}$) than what could be expected if the combined effect of all particles consisted in the superposition of their individual effects (proportional to $\Phi$). The wall-normal velocity fluctuations systematically increase with $\Phi$ in the particle-free upper regions of the duct while displaying an increase at lower $\Phi$ and decrease at larger $\Phi$ in the lower regions of the duct. The above observations are qualitatively similar to the channel flow DNSs of Shao *et al.* [9]: In the near-wall region, the presence of particles disrupts the larger coherent flow structures, e.g., high- or low-speed streaks, and thus reduces the streamwise turbulence intensity (see also [8,33]). On the other hand, particle-induced small-scale vortices in the near-wall region increase the wall-normal (and spanwise, not measured here) velocity fluctuations. At larger volume fractions, sufficient to cover the bottom wall with particles (corresponding to $\Phi \approx 4.5\%$ for SPs and 7% for LPs considering that all particles settle on the bottom wall at maximum packing, assumed here as 65%), the particle layer behaves like a rough wall. Vortices that are shed as the fluid moves above this particle-wall layer are transported towards the core, leading to an enhancement of the fluid velocity fluctuations in that region, as evident in Fig. 9 and also found in [9].

### 3. Particle distribution and relative velocity field

The ability to track individual particles and their neighbors, within the area of observation, makes it possible to extract particle-centered statistics. This enables us to investigate the dynamics of neighboring particles surrounding a reference particle. Accordingly, the particle-centered distribution function and relative velocity are shown in Figs. 10 and 11 for the lowest and highest $\Phi$, respectively. The flow is from the left to right. Since the flow is nonhomogeneous in the wall-normal direction, these distribution functions are plotted for three elevations $y$, centered at $y_i = d_p/2$, $3d_p/2$, and $5d_p/2$, i.e., the first, second, and third particle layers, respectively, corresponding to the three rows in Figs. 10 and 11. In the $x$-$y$ measurement plane, the particle-centered distribution function for each elevation $y_i$ is defined as

$$\sum_{n=1}^{N_i} M_i(x - x_p, y - y_p)/N_i \ \forall \ y_p \in (y_i - d_p/2, y_i + d_p/2).$$

Here $M_i(x - x_p, y - y_p)$ is the mask matrix centered around a reference particle whose centroid is located at $(x_p, y_p)$. Further, $M_i(x - x_p, y - y_p)$ has a value equal to 1 in the solid phase and 0 in the fluid phase. The averaging is performed over all $N_i$ reference particles whose centroid's wall-normal position $y_p$ lies inside the region $(y_i - d_p/2, y_i + d_p/2)$, i.e., in a band that is one particle diameter thick, and over all PIV images. The particle-centered relative velocity distribution
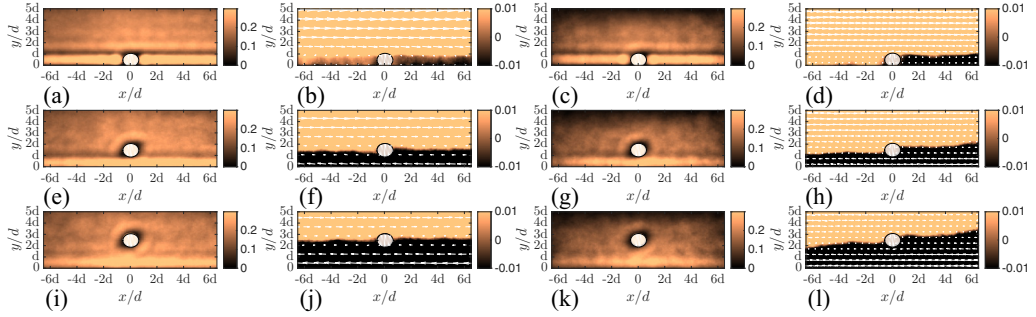
FIG. 11. Particle-centered distribution and relative velocity field at $\Phi = 5\%$. The details are the same as in Fig. 10.

is similarly calculated by subtracting the velocity of the reference particle from all the neighboring particles' velocity.

In Figs. 10 and 11, the first two columns correspond to the distribution function and the streamwise relative velocity for the SPs. Similarly, the last two columns correspond to the LPs. The distances are scaled by the corresponding particle diameter, so the last two columns are actually representing a larger physical area as compared to the first two columns due to the larger size of LPs.

From the distribution function for the bottom layer at $\Phi = 1\%$ [Figs. 10(a)–10(e) and 10(i)], it is evident that, on average, there is a region of high concentration immediately behind and in front of the reference particle. There is also a noticeably higher concentration in the top left part. A small region with very low particle concentration appears in the bottom left and top right neighborhoods of the reference particle. This particle-depleted region is perhaps more strongly visible in the second layer of SPs [Figs. 10(a) and 10(e)–10(i)]. This preferential alignment of the particle-rich and particle-depleted regions is due to particle inertia, quantified by the particle Reynolds number proportional to $\dot{\gamma} d_p^2/\nu_f$, where $\dot{\gamma}$ is the mean shear rate. Picano *et al.* [39] showed that larger particle inertia can lead to larger excluded volume around the particle and thus shear-induced thickening. The effects of particle inertia, now defined based on the relative slip velocity ($U_f - U_p$), manifests in the relative velocity distribution (second and fourth columns in Fig. 10), especially for the bottom layer, where particles behind the reference particles are *drafted* towards it and the velocity distribution is reminiscent of the wake behind a solid body. The larger noise in the statistics of LPs is due to their smaller number at a given $\Phi$.

The above trends for $\Phi = 1\%$ are in general preserved at higher $\Phi = 5\%$ (see the first and third columns of Fig. 11). Here the particle-rich and particle-depleted regions can be clearly observed for the second and third layers [Figs. 11(e)–11(h) and Figs. 11(i)–11(l)]. Also the wake behind the reference particle is prominently seen across all three particle layers (see the second and fourth columns of Fig. 11), especially for LPs, which could be due to their larger inertia. For the bottom layer of particles, in contrast to the case for lower $\Phi = 1\%$, the distribution function displays higher symmetry about the vertical line $x/d = 0$, especially for SPs. This is most likely because of the significantly higher particle concentration in the bottom layer leading to more frequent collisions and hence a more uniform concentration.

### 4. Particle cluster formation

The particle-centered distribution function shown in Figs. 10 and 11 reflects the average spatial distribution of neighboring particles. Moreover, instantaneous visualizations of the particle distribution indicate the formation of occasional trainlike clusters as shown in Fig. 12(a), along with instances where the spacing between neighboring particles is nearly uniform [Fig. 12(b)]

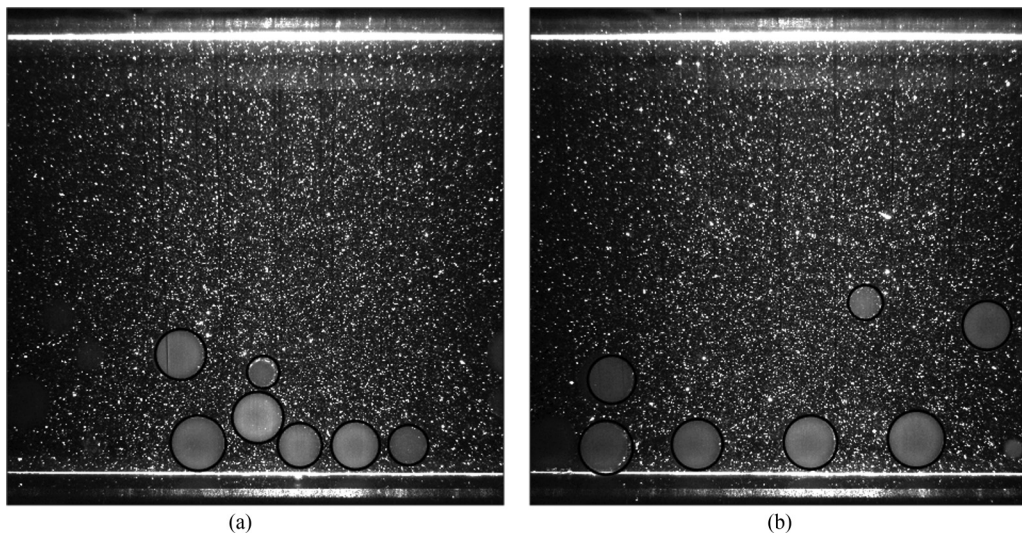(a)                                               (b)

FIG. 12. (a) Particles occasionally moving in a trainlike cluster and (b) particles moving with nearly constant relative spacing. These instances correspond to LPs at $\Phi = 3\%$.

and instances when the spacing between neighboring particles is larger than average (not shown). The probability distribution function (PDF) of the center-to-center distance between neighboring particles provides evidence about the existence of such clusters. If the distance between neighboring particles remains nearly constant, then the PDF should display a peak around the average spacing. This average spacing must decrease with particle concentration and approach a minimum value of one particle diameter when all particles move in contact as a packed bed at the maximum packing fraction.

Figure 13(a) and 13(b) show the PDF of the center-to-center distance between neighboring particles for the bottom layer of SPs and LPs. The PDF has been normalized so that the area under the curve $\sum_{\Delta x/d} \text{PDF} \times \Delta(\Delta x/d)$ equals 1. The average spacing, calculated as the mean value



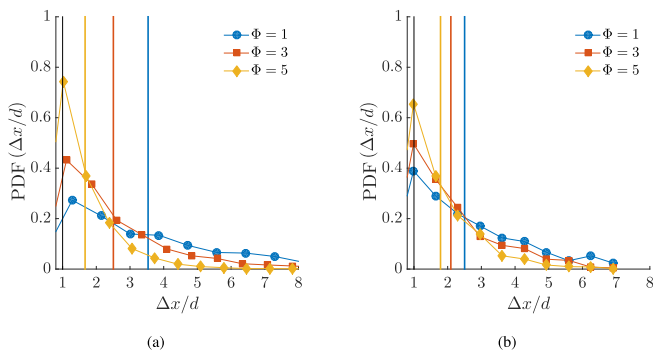(a)                                               (b)

FIG. 13. Probability distribution function of the center-to-center separation distance between neighboring particles in the bottom near-wall layer for (a) smaller particles and (b) larger particles. The vertical lines (the same color corresponds to the same volume fraction) correspond to the average spacing denoting a scenario where the particles would move with a constant relative spacing. The black vertical line corresponds to a separation distance of one particle diameter corresponding to the scenario where all neighboring particles are in contact and move as a continuous train.

of the PDF

$$\sum_{\Delta x/d} \text{PDF} \times \Delta x/d \times \Delta(\Delta x/d),$$

decreases with increasing $\Phi$ and is represented with a vertical line in Figs. 13(a) and 13(b). The peak of the PDF, or the modal value, is shifted towards distances smaller than the average spacing in the bottom near-wall layer, indicating a tendency for two or more particles to travel with smaller than average relative spacing between them, i.e., trainlike clusters exist. This cluster formation could be due to (i) the drafting motion behind the reference particle as seen in Figs. 10 and 11 where particles following the reference particle are attracted in its wake (see also [40]) and (ii) the tendency of particles to sample low-speed streaks (as seen in [9,10]). Cisse *et al.* [14] proposed that in the case of finite-size particle clustering, mostly particles on the surface of the cluster affect the global flow statistics. One can also see separation distances smaller than one particle diameter, which is an effect caused by the partial illumination of the spherical particles by the thin laser light sheet, discussed before, making the particles appear as smaller spheres.

## V. CONCLUSION

We have considered the turbulent flow of a particle suspension in a square duct and have presented fluid-particle velocity and concentration statistics using RIM PIV experiments for two different particle sizes (14.5 and 9 in terms of ratio between the duct height and particle diameter) and volume fractions $\Phi$ from 1% to 5%. The pressure drop increases with $\Phi$ but, within the error bars, it is insensitive to the particle size for the range of $\Phi$ and Reynolds numbers $\text{Re}_{2H}$ considered in this study. However, the fluid turbulent velocity statistics are considerably different for the two particle sizes, the effects with respect to the single-phase flow being more pronounced for smaller particles owing to their larger number. We therefore suggest that two competing mechanisms are active in these flows, where the total pressure drop is given by the viscous stress at the wall and by the friction caused by the particles sliding on the wall. Thus, on one side, smaller particles are characterized by a lower wall viscous stress as they form a less permeable bed; on the other side, a more packed bed (smaller particles) is associated with higher drag and more contact points with the bottom wall. In particular, the mean velocity profiles look fuller for large particles and fluctuations are more intense for smaller particles. These two effects appear to balance, yielding a similar global pressure drop.

Moreover, the secondary flow intensity is found to increase in the presence of particles. Particle-centered distributions have identified regions with high and low concentration in the vicinity of the reference particle. This excluded volume manifests due to the finite inertia at the particle scale. Also, relative velocity distributions have shown the existence of wakelike regions behind the reference particle in the near-wall region. Trailing particles attracted in this wake zone along with particle segregation in low-speed regions might be the reason for the observed particle clustering.

Almost excellent quantitative agreement is seen between the turbulent statistics obtained from fully resolved DNSs and experiments for the case with small particles at $\Phi = 1\%$ thus corroborating both methods in such a complex flow setting. Good agreement between simulations and experiments despite not exactly matching values for collision parameters (e.g., coefficient of friction and restitution) indicate that, in turbulent flows, the results are not significantly affected by these variables. We hope that these high-resolution velocity and concentration measurements may serve as an experimental data set to provide new insights into the modification of turbulence induced by the presence of a mobile sediment bed, in the same spirit as the work of Revil-Baudard *et al.* [41] and Ni and Capart [42].

## ACKNOWLEDGMENTS

---

[1] C. T. Crowe, J. D. Schwarzkopf, M. Sommerfeld, and Y. Tsuji, *Multiphase Flows with Droplets and Particles* (CRC, Boca Raton, 2011).

[2] S. Balachandar and J. K. Eaton, Turbulent dispersed multiphase flow, Annu. Rev. Fluid Mech. **42**, 111 (2010).

[3] J. Yao and M. Fairweather, Inertial particle resuspension in a turbulent, square duct flow, Phys. Fluids **22**, 033303 (2010).

[4] C. M. Winkler, S. L. Rani, and S. P. Vanka, Preferential concentration of particles in a fully developed turbulent square duct flow, Int. J. Multiphase Flow **30**, 27 (2004).

[5] G. Sharma and D. J. Phares, Turbulent transport of particles in a straight square duct, Int. J. Multiphase Flow **32**, 823 (2006).

[6] A. Soldati and C. Marchioli, Physics and modeling of turbulent particle deposition and entrainment: Review of a systematic study, Int. J. Multiphase Flow **35**, 827 (2009).

[7] Z.-W. Lin, X.-M. Shao, Z.-S. Yu, and L.-P. Wang, Effects of finite-size heavy particles on the turbulent flows in a square duct, J. Hydrodyn. **29**, 272 (2017).

[8] W. Fornari, H. T. Kazerooni, J. Hussong, and L. Brandt, Suspensions of finite-size neutrally buoyant spheres in turbulent duct flow, J. Fluid Mech. **851**, 148 (2018).

[9] X. Shao, T. Wu, and Z. Yu, Fully resolved numerical simulation of particle-laden turbulent flow in a horizontal channel at a low Reynolds number, J. Fluid Mech. **693**, 319 (2012).

[10] A. G. Kidanemariam, C. Chan-Braun, T. Doychev, and M. Uhlmann, Direct numerical simulation of horizontal open channel flow with finite-size, heavy particles at low solid volume fraction, New J. Phys. **15**, 025031 (2013).

[11] C. Poelma, J. Westerweel, and G. Ooms, Turbulence statistics from optical whole-field measurements in particle-laden turbulence, Exp. Fluids **40**, 347 (2006).

[12] S. Wiederseiner, N. Andreini, G. Epely-Chauvin, and C. Ancey, Refractive-index and density matching in concentrated particle suspensions: A review, Exp. Fluids **50**, 1183 (2011).

[13] S. Klein, M. Gibert, A. Bérut, and E. Bodenschatz, Simultaneous 3D measurement of the translation and rotation of finite-size particles and the flow field in a fully developed turbulent water flow, Meas. Sci. Technol. **24**, 024006 (2012).

[14] M. Cisse, E.-W. Saw, M. Gibert, E. Bodenschatz, and J. Bec, Turbulence attenuation by large neutrally buoyant particles, Phys. Fluids **27**, 061702 (2015).

[15] M. L. Byron and E. A. Variano, Refractive-index-matched hydrogel materials for measuring flow-structure interactions, Exp. Fluids **54**, 1456 (2013).

[16] H. M. D. Harshani, S. A. Galindo-Torres, A. Scheuermann, and H. B. Muhlhaus, Experimental study of porous media flow using hydro-gel beads and LED based PIV, Meas. Sci. Technol. **28**, 015902 (2016).

[17] J. A. Dijksman, N. Brodu, and R. P. Behringer, Refractive index matched scanning and detection of soft particles, Rev. Sci. Instrum. **88**, 051807 (2017).

[18] A. A. Draad, G. D. C. Kuiken, and F. T. M. Nieuwstadt, Laminar-turbulent transition in pipe flow for Newtonian and non-Newtonian fluids, J. Fluid Mech. **377**, 267 (1998).

[19] S. Zade, P. Costa, W. Fornari, F. Lundell, and L. Brandt, Experimental investigation of turbulent suspensions of spherical particles in a square duct, J. Fluid Mech. **857**, 748 (2018).

[20] T. Leeungculsatien and G. P. Lucas, Measurement of velocity profiles in multiphase flow using a multi-electrode electromagnetic flow meter, Flow Meas. Instrum. **31**, 86 (2013).

[21] W. Fornari, F. Picano, and L. Brandt, The effect of polydispersity in a turbulent channel flow laden with finite-size particles, Eur. J. Mech. B **67**, 54 (2018).

[22] T. A. Johnson and V. C. Patel, Flow past a sphere up to a Reynolds number of 300, J. Fluid Mech. **378**, 19 (1999).

[23] R. Clift, J. R. Grace, and M. E. Weber, *Bubbles, Drops, and Particles* (Courier, Chelmsford, 2005).

[24] P. Gondret, M. Lance, and L. Petit, Bouncing motion of spherical particles in fluids, Phys. Fluids **14**, 643 (2002).

[25] G. G. Joseph, R. Zenit, M. L. Hunt, and A. M. Rosenwinkel, Particle-wall collisions in a viscous fluid, J. Fluid Mech. **433**, 329 (2001).

[26] M. Raffel, C. E. Willert, S. T. Wereley, and J. Kompenhans, *Particle Image Velocimetry: A Practical Guide* (Springer, Berlin, 2013).

[27] T. Kawata and S. Obi, Velocity-pressure correlation measurement based on planar PIV and miniature static pressure probes, Exp. Fluids **55**, 1776 (2014).

[28] S. Wereley and L. Gui, A correlation-based central difference image correction (CDIC) method and application in a four-roll mill flow PIV measurement, Exp. Fluids **34**, 42 (2003).

[29] K. Okamoto, S. Nishio, T. Saga, and T. Kobayashi, Standard images for particle-image velocimetry, Meas. Sci. Technol. **11**, 685 (2000).

[30] H. K. Yuen, J. Princen, J. Illingworth, and J. Kittler, Comparative study of Hough transform methods for circle finding, Image Vis. Comput. **8**, 71 (1990).

[31] W.-P. Breugem, A second-order accurate immersed boundary method for fully resolved simulations of particle-laden flows, J. Comput. Phys. **231**, 4469 (2012).

[32] H. Brenner, The slow motion of a sphere through a viscous fluid towards a plane surface, Chem. Eng. Sci. **16**, 242 (1961).

[33] F. Picano, W.-P. Breugem, and L. Brandt, Turbulent channel flow of dense suspensions of neutrally buoyant spheres, J. Fluid Mech. **764**, 463 (2015).

[34] P. Costa, F. Picano, L. Brandt, and W.-P. Breugem, Effects of the finite particle size in turbulent wall-bounded flows of dense suspensions, J. Fluid Mech. **843**, 450 (2018).

[35] S. Gavrilakis, Numerical simulation of low-Reynolds-number turbulent flow through a straight square duct, J. Fluid Mech. **244**, 101 (1992).

[36] R. A. Bagnold, The flow of cohesionless grains in fluids, Philos. Trans. R. Soc. London Ser. A **249**, 235 (1956).

[37] B. W. Borsje *et al.*, The role of suspended load transport in the occurrence of tidal sand waves, J. Geophys. Res.: Earth Surface **119**, 701 (2014).

[38] J. Fredsøe and R. Deigaard, *Mechanics of Coastal Sediment Transport* (World Scientific, Singapore, 1992).

[39] F. Picano, W.-P. Breugem, D. Mitra, and L. Brandt, Shear Thickening in Non-Brownian Suspensions: An Excluded Volume Effect, Phys. Rev. Lett. **111**, 098302 (2013).

[40] J.-P. Matas, V. Glezer, É. Guazzelli, and J. F. Morris, Trains of particles in finite-Reynolds-number pipe flow, Phys. Fluids **16**, 4192 (2004).

[41] T. Revil-Baudard, J. Chauchat, D. Hurther, and O. Eiff, Turbulence modifications induced by the bed mobility in intense sediment-laden flows, J. Fluid Mech. **808**, 469 (2016).

[42] W.-J. Ni and H. Capart, Stresses and drag in turbulent bed load from refractive index-matched experiments, Geophys. Res. Lett. **45**, 7000 (2018).